Ellipsometric measurement of universal critical adsorption integrals

Dan S. P. Smith and Bruce M. Law
Department of Physics, Kansas State University, Manhattan, Kansas 66506-2601
(Received 19 September 1994)

We present an experimental determination of the universal critical adsorption integrals $\int P_+ = \int P_+(x)dx$ and $\int P_- = \int [P_-(x)-1]dx$, where $P_\pm(x)$ are the one-phase (+) and the two-phase (−) universal functions that scale the variation of the local order parameter near a free surface in the vicinity of the Ising critical end point. From ellipsometric measurements on three critical binary liquid mixtures we obtain $\int P_+ = 1.86 \pm 0.11$, $\int P_- = 1.61 \pm 0.04$, and $R_{MA} = 1.19 \pm 0.04$ for their ratio, where the quoted uncertainties represent one standard deviation. These values are compared with recent theoretical and computational results. The renormalization-group calculation of Diehl and Smock [Phys. Rev. B **47**, 5841 (1993)] obtained $\int P_+ = 1.91$, $\int P_- = 1.44$, and $R_{MA} = 1.33$, while a Monte Carlo simulation [M. Smock, H. W. Diehl, and D. P. Landau, Ber. Bunsenges. Phys. Chem. **98**, 486 (1994)] obtained $\int P_+ = 2.18$, $\int P_- = 1.97$, and $R_{MA} = 1.11$. An interpolation to dimension $d = 3$ of exact calculations for $d = 2$ and 4 [G. Flöter and S. Dietrich, Z. Phys. B **97**, 213 (1995)] obtained $\int P_+ = 2.27 \pm 0.33$, $\int P_- = 1.84 \pm 0.33$, and $R_{MA} = 1.32 \pm 0.07$.

PACS number(s): 68.10.−m, 64.60.Fr, 05.70.Jk, 82.65.Dp

I. INTRODUCTION

When a critical binary liquid mixture approaches the bulk phase transition, critical behavior is induced at the noncritical liquid-vapor or liquid-solid surfaces. Let L and H be the two molecular components of the mixture, L (H) being the component having the pure state with lower (higher) density. At all temperatures the component with the lower surface tension is preferentially adsorbed at the surface. As T_c, the bulk critical temperature, is approached from either above or below, the thickness of this adsorption profile diverges proportional to the correlation length. This phenomenon, known as critical adsorption, is described by the local order parameter's variation with depth into the surface,

$$m(z,t) = \varphi_L(z,t) - \varphi_L(+\infty,0), \quad z \geq 0 . \tag{1}$$

Here z is zero at the surface and positive in the liquid. $\varphi_L(z,t)$ is the local volume fraction and $\varphi_L(+\infty,0)$ is the bulk critical volume fraction of the L component, while $t = |T - T_c|/T_c$ is the reduced temperature.

As the critical temperature is approached from the one-phase (subscript +) or the two-phase (subscript −) region, the critical adsorption profile at the liquid-vapor surface scales as

$$m_\pm(z,t) = M_- t^\beta P_\pm \left[\frac{z + z_e}{\xi_\pm} \right] , \tag{2}$$

where the surface scaling functions $P_+(x)$ and $P_-(x)$ have different forms, but are both universal. Here β and M_- are the usual critical exponent and coefficient of the bulk order parameter in the two-phase region $m_-(+\infty,t) = M_- t^\beta$. The extrapolation length z_e is nonuniversal and independent of t and z. The bulk correlation length $\xi_\pm = \xi_{0\pm} t^{-\nu}$ has the universal amplitude ratio [1]

$$\frac{\xi_{0+}}{\xi_{0-}} = 1.96 . \tag{3}$$

Taking into account Eq. (3), the nonuniversal behavior in Eq. (2) arises solely from the two bulk amplitudes ξ_{0+} and M_- and the surface parameter z_e. Equation (2) assumes that component L is preferentially adsorbed at the surface. If instead H is preferentially adsorbed, then the critical adsorption profile at the liquid-vapor surface would be

$$m_+(z,t) = -M_- t^\beta P_+ \left[\frac{z + z_e}{\xi_+} \right] . \tag{4}$$

This equation only holds in the one-phase region. The scaling function $P_+(x)$ in Eqs. (2) and (4) are expected to be identical. In Ref. [2] we discuss certain unsatisfactory aspects of scaling for the case in which the heavier component H is adsorbed at the upper liquid-vapor surface in the two-phase region. This case is not experimentally studied in this publication.

Equation (2) was originally derived using mean-field theory [3], where the solutions are

$$P_+(x) = 2^{1/2}\mathrm{csch}(x) , \tag{5}$$

$$P_-(x) = \coth(x/2) . \tag{6}$$

Equations (2), (5), and (6) correctly imply that the surface is ordered both above and below T_c. Although the surface is not undergoing an ordering transition at T_c, the ordering transition occurring in the bulk stimulates the critical scaling at the surface.

Fisher and de Gennes [4] supported Eq. (2) using scaling arguments valid beyond mean-field theory. They proposed that the scaling functions have the limits

$$P_{\pm}(x)-P_{\pm}(\infty)\cong P_{\infty,\pm}e^{-x} \tag{7}$$

for $x \gg 1$, with $P_{+}(\infty)=0$ and $P_{-}(\infty)=1$, and

$$P_{\pm}(x)\cong c_{\pm}x^{-\beta/\nu} \tag{8}$$

for $x \ll 1$, where $P_{\infty,\pm}$ and $c_{\pm}$ are universal constants. The scaling in Eq. (2) has been tested extensively using a variety of experimental probes [5]. Reflectometry [6,7] and ellipsometry [6,8,9] studies have verified the exponential decay of Eq. (7) beyond doubt and have provided evidence of the power-law behavior of Eq. (8) for small x. These studies were testing theoretical functions $P_{\pm}(x)$ with the correct *asymptotic forms,* but with multiple adjustable parameters. They were unable to pinpoint the scaling functions quantitatively over the entire range of x.

More recently theoretical determinations of the scaling functions with zero adjustable parameters have become available. Diehl and Smock [10] have published a renormalization-group one-loop calculation for $P_{\pm}(x)$, while Smock, Diehl, and Landau [11] have fitted functions $P_{\pm}(x)$ to the Monte Carlo data of Landau and Binder [12]. In addition, Flöter and Dietrich [13] have provided universal quantities related to critical adsorption with an interpolation to dimension $d=3$ of exact calculations for $d=2$ and 4. The purpose of this paper is to provide an experimental test of these three recent theories.

Over the past four years we have used ellipsometry to study critical adsorption at the liquid-vapor surface of seven different critical binary liquid mixtures: cyclohexane-methanol (CM) [14]; aniline-cyclohexane (AC) and isobutyric acid–water (IW) [15]; hexadecane-acetone (HA) [16]; nitrobenzene–*n*-hexane (NH), 2,6 lutidine–water (LW), and 3-methylpyridine–D_2O (PD) [17]. The mixtures CM and HA undergo wetting in the two-phase region, so that critical adsorption was studied only in the one-phase region. For the other five mixtures both the one, and the two-phase regions were studied. For LW and PD the measurements were taken near the lower critical point, while the measurements on all the other samples were taken near the upper critical point. In Refs. [15] and [17] we used the ellipsometric measurements for AC, IW, NH, LW, and PD to determine an experimental value for the universal ratio

$$R_{MA}=\frac{\int P_{+}}{\int P_{-}}\ , \tag{9}$$

where

$$\int P_{+}=\int_{0}^{+\infty}P_{+}(x)dx \tag{10}$$

and

$$\int P_{-}=\int_{0}^{+\infty}[P_{-}(x)-1]dx\ . \tag{11}$$

In this paper we present a more sophisticated modification of this analysis and obtain separate measurements of the universal integrals $\int P_{+}$ and $\int P_{-}$ for our seven mixtures. We also obtain $\int P_{+}$ for the one-phase ellipsometric data taken by Schmidt [8] on the upper critical point mixture methylcyclohexane (C_7H_{14})-perfluoromethylcyclohexane (C_7F_{14}), which will be referred to as Sch. In order to derive values for $\int P_{\pm}$ from the ellipsometric data, experimental values for the bulk amplitudes ξ_{0+} and M_{-} are required. The ratio R_{MA} is less fundamental, but has the advantage of being independent of these system-dependent amplitudes.

In Sec. II we compare the theoretical functions $P_{\pm}(x)$ from the renormalization-group calculation of Ref. [10] with the Monte Carlo simulation of Ref. [11]. In Sec. III we incorporate $P_{\pm}(x)$ into a model of the optical dielectric surface profile $\varepsilon(z,t)$, while in Sec. IV we use this model $\varepsilon(z,t)$ profile to derive a relation between the ellipsometric data and the universal integrals $\int P_{\pm}$. The details of this derivation are provided in Appendixes A and B. The relevant experimental details are discussed in Sec. V. In Sec. VI we present experimental values for $\int P_{\pm}$ and analyze the accuracy of our method of extracting these universal integrals from the experimental data. Finally, in Sec. VII we summarize the results and draw conclusions from our experimental study. Our most reliable ellipsometric data are provided in Appendix C.

II. THEORETICAL SURFACE SCALING FUNCTIONS $P_{\pm}(x)$

Figures 1(a) and 1(b) show the theoretical scaling functions $P_{\pm}(x)$, defined in Eq. (2), for the mean-field (dashed line), the renormalization-group (RG, solid line), and the Monte Carlo (MC, solid line) simulation. The mean-field profiles are from Eqs. (5) and (6). The universal integrals $\int P_{\pm}$ over the mean-field profiles are infinite, as defined in Eqs. (10) and (11).

Diehl and Smock [10] published the scaling functions $P_{\pm}(x)$ for the renormalization-group one-loop calculation in dimension $d=4-\varepsilon$. These functions are shown in Figs. 1(a) and 1(b) for $d=3$. For the $x\to 0$ asymptotic region they obtained

$$P_{+}(x)\sim 0.717x^{-1/2}\ , \tag{12}$$

$$P_{-}(x)\sim 1.113x^{-1/2}\ . \tag{13}$$

In Eqs. (12) and (13) the expected β/ν exponent has been set to its approximate value of 0.5 and higher-order terms have been neglected. For the $x\to\infty$ asymptotic region they obtain

$$P_{+}(x)\sim 1.621e^{-x}\ , \tag{14}$$

$$P_{-}(x)-1\sim(0.028+0.0098x)e^{-x}\ . \tag{15}$$

The results (12)–(15), along with tabled $P_{\pm}(x)$ values, were supplied to us by Diehl and Smock. After comparing the tabled $P_{\pm}(x)$ values with the asymptotic functions (12)–(15), we concluded that the upper limit for the $x\to 0$ asymptotic behavior was approximately $x_1\cong 0.5$, while the lower limit for the $x\to\infty$ asymptotic behavior was approximately $x_2\cong 3$.

To determine the integrals $\int P_{\pm}$, we integrated Eqs. (12)–(15) over the above-mentioned asymptotic regions and used Diehl and Smock's numerical values for $P_{\pm}(x)$

to estimate the integrals over the crossover region in between. For the renormalization-group functions, we obtain $\int P_+ = 1.91$, $\int P_- = 1.44$, and $R_{MA} = 1.33$ for the universal quantities defined in Eq. (9)–(11).

Burkhardt and Diehl [18] prove the exact equivalence between critical adsorption and the extraordinary transition for magnetic systems. Landau and Binder [12] have published a Monte Carlo study for the extraordinary transition in an Ising film. Smock, Diehl, and Landau applied the scaling of Eq. (2) to these data and obtained fitted scaling functions $P_\pm(x)$ [11]. These functions were provided to us in tabled form, along with the $x \to 0$, asymptotic results

$$P_+(x) \sim 0.866 x^{-\beta/\nu}, \tag{16}$$

$$P_-(x) \sim 1.22 x^{-\beta/\nu}. \tag{17}$$

From the tabled $P_\pm(x)$ values we estimated the $x \to \infty$ asymptotic forms

$$P_+(x) \sim 1.5 e^{-x}, \tag{18}$$

$$P_-(x) - 1 \sim 1.0 e^{-x}. \tag{19}$$

For these Monte Carlo results we concluded that the upper limit for the $x \to 0$ asymptotic behavior was approximately $x_1 \cong 0.2$, while the lower limit for the $x \to \infty$ asymptotic behavior was approximately $x_2 \cong 1$. Using the method of integration described for the Diehl and Smock functions above, we obtain $\int P_+ = 2.18$, $\int P_- = 1.97$, and $R_{MA} = 1.11$ for the Monte Carlo functions.

A comparison of Eqs. (12)–(15) with (16)–(19) demonstrates that the two theories are in reasonable agreement for the values of $c_\pm$ and $P_{+,\infty}$, but not for $P_{-,\infty}$. Figures 2(a) and 2(b) are semilogarithmic plots of $P_+(x)$ and $P_-(x) - 1$, where the exponential decay region can be clearly seen. The renormalization-group and Monte Car-

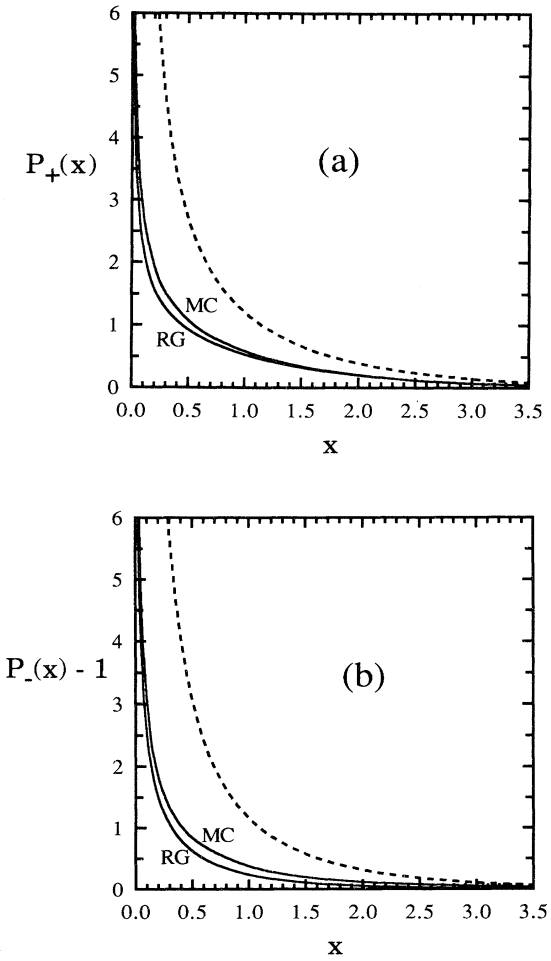

FIG. 1. Graphs showing the theoretical universal surface scaling functions (a) $P_+(x)$ and (b) $P_-(x) - 1$. The functions are represented by dashed lines for the mean-field theory and solid lines for the renormalization-group and Monte Carlo theories, labeled RG and MC, respectively.

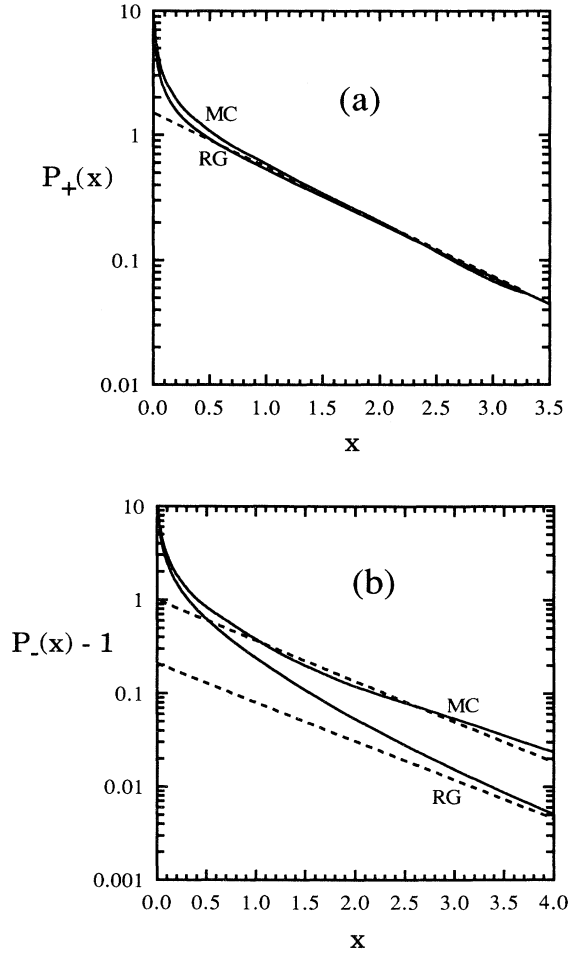

FIG. 2. Semilogarithmic plots of the scaling functions (a) $P_+(x)$ and (b) $P_-(x) - 1$. The solid lines show the theoretical renormalization-group and Monte Carlo scaling functions, labeled RG and MC, respectively. The straight dashed lines are the Monte Carlo asymptotic exponential functions given by Eqs. (18) and (19) and the renormalization-group asymptotic exponential function given by Eq. (15) in (b).

lo scaling functions are represented by the solid lines, labeled RG and MC, respectively. The Monte Carlo asymptotic functions of Eqs. (18) and (19) are represented by dashed lines and the renormalization-group asymptotic function of Eq. (15) is represented by the lower dashed line in Fig. 2(b). The asymptotic functions are straight lines with y intercepts of $P_{\pm,\infty}$, but with slopes independent of $P_{\pm,\infty}$. Figure 2(a) shows the strong agreement for $P_{+,\infty}$, while Fig. 2(b) shows the strong disagreement for $P_{-,\infty}$ between the two theories. In Fig. 2(b) we observe that the renormalization-group profile approaches its asymptotic behavior very slowly, while the Monte Carlo profile oscillates about the exponential function given by Eq. (19). This latter effect could be due to finite-size effects in the Monte Carlo simulation.

A third set of theoretical results by Flöter and Dietrich [13] calculates critical adsorption quantities for dimension $d=3$ by interpolation using exact results for $d=2$ and 4. They obtained $c_+=0.94\pm0.05$ and $c_-=1.24\pm0.05$, in reasonable agreement with the Monte Carlo values in Eqs. (16) and (17). They also obtained the universal quantities $g_\pm$ and R_Φ, related to the quantities of Eqs. (9)–(11) through the relations $\int P_\pm = g_\pm/(\nu-\beta)$ and $R_{MA}=R_\Phi \xi_{0-}/\xi_{0+}$. Using their results in these relations we obtain $\int P_+ = 2.27\pm0.33$, $\int P_- = 1.84\pm0.33$, and $R_{MA}=1.32\pm0.07$. Given the large uncertainties on the $\int P_\pm$ values, these individual integrals are in agreement with the Monte Carlo results. However, the R_{MA} result is in much better agreement with the renormalization-group value.

The scaling functions $P_\pm(x)$ become infinite as $x\to 0$. If the extrapolation length z_e in Eq. (2) were zero, $m(0,t)$ would be infinite, which is physically unreasonable. Equation (1) provides a stronger limit on the order parameter at the surface $m(0,t)$. The volume fraction of component L at the surface $\varphi_L(0,t)$ has a lower limit of 0 and an upper limit of 1, corresponding respectively, to a layer of pure H or pure L at the liquid-vapor surface. Consequently, according to Eq. (1),

$$-\varphi_L(+\infty,0)\le m(0,t)\le 1-\varphi_L(+\infty,0)\ . \tag{20}$$

The component L or H that has the lower liquid-vapor surface tension in the pure state is preferentially adsorbed at the liquid-vapor surface of the mixture. The upper limit in Eq. (20) is relevant if component L is preferentially adsorbed. The mixtures for which this is the case will be referred to as group L. The mixtures AC, IW, LW, NH, and PD belong to this group. The lower limit in Eq. (20) is relevant if component H is preferentially adsorbed. We call this group H, which includes CM, HA, and Sch.

If we apply Eq. (20) to Eq. (2) for group L or to Eq. (4) for group H, we obtain

$$P_\pm(z_e/\xi_\pm)\le \frac{1-\varphi_i(+\infty,0)}{M_- t^\beta}\ , \tag{21}$$

where $i=L$ (H) for group L (H). Equation (4) applies to the one-phase region only, therefore Eq. (21) is only valid in the one-phase region for group H. Equation (21) provides a lower limit $z_{e\,\min}$ on z_e. We will set $z_e=z_{e\,\min}$. For all eight mixtures, the value of the right-hand side of Eq. (21) is large enough over the range of reduced temperatures studied that the asymptotic form of Eq. (8) can be applied approximately to $P_\pm(z_{e\,\min}/\xi_\pm)$. Using Eq. (8) in Eq. (21) we obtain

$$z_e\cong z_{e\,\min}=\xi_{0\pm}\left[\frac{1-\varphi_i(+\infty,0)}{c_\pm M_-}\right]^{-\nu/\beta}\ . \tag{22}$$

In Eq. (22), z_e is independent of reduced temperature. Furthermore, z_e has the same value in the one- and the two-phase region because of the relation [10]

$$\xi_{0+}(c_+)^{\nu/\beta}=\xi_{0-}(c_-)^{\nu/\beta}\ . \tag{23}$$

In Table I, values of z_e implied by Eq. (22) are given for each liquid mixture. The value for c_+ was taken from Eq. (16). Values and references for the parameters ξ_{0+}, $\varphi_L(+\infty,0)$, and M_- are provided in Table II.

III. OPTICAL DIELECTRIC PROFILE $\varepsilon(z,t)$

The local order parameter $m(z,t)$ is commonly converted to the optical dielectric profile $\varepsilon(z,t)$ by use of the two-component Clausius-Mossotti relation [19]

$$\varphi_L(z,t)\eta_L+[1-\varphi_L(z,t)]\eta_H\cong\eta(z,t)\ , \tag{24}$$

TABLE I. Values of the liquid mixture quantities that must be small in order that the approximations in this paper are valid.

Mixture	z_e (10^{-10} m)	$\Delta_{\max}$	First-order correction in $\Delta(z,t)$ of Eq. (A2)	$R_V(0)$
AC	13.1	−0.025	−0.004	0.59
IW	6.58	0.017	−0.002	−0.33
LW	3.30	0.058	−0.004	−0.64
NH	10.4	−0.035	−0.002	0.98
PD	2.56	0.058	−0.003	−0.58
CM	3.04	−0.043	0.0006	0.44
HA	6.43	−0.020	0.0007	0.36
Sch	7.55	−0.038	0.005	0.61

TABLE II. Nonuniversal parameters required for the analysis of the eight binary liquid mixtures studied in this paper.

Mixture	ε_H[a]	ε_L[a]	M_-	ξ_{0+} (Å)	ξ_V (Å)[b]	$\varphi_L(+\infty,0)$
AC	2.5163	2.0924	1.03±0.03[c]	2.3±0.2[d]	1.7	0.639[e]
IW	1.773	1.94	0.783±0.03[f]	3.63±0.07[e]	1.7	0.502[g]
LW	1.773	2.217[h]	0.931±0.007[i]	2.5±0.3[j]	1.8	0.3015[k]
NH	2.4218	1.8909	0.770±0.006[l]	3.54±0.12[m]	1.95	0.619[n]
PD	1.80	2.25	0.558±0.007[o]	5.2±0.5[p]	1.91	0.3103[k]
CM	1.766	2.0924	0.755±0.003[q]	3.24±0.23[q]	1.98	0.676[q]
HA	1.8463	2.0578	1.02±0.005[r]	2.0±0.2[p]	1.59	0.482[r]
Sch	1.651	2.025	0.968±0.009[s]	2.79±0.3[t]	2.57	0.50[t]

[a]Reference [28], except where noted.
[b]See Appendix B.
[c]References [29,30].
[d]References [29,31].
[e]Reference [29].
[f]Reference [19].
[g]Reference [32].
[h]Reference [33].
[i]Reference [34].
[j]Reference [35].
[k]Reference [17].
[l]References [30,36].
[m]Reference [37].
[n]Reference [36].
[o]Reference [38].
[p]Reference [24].
[q]Reference [39].
[r]Reference [40].
[s]Reference [41].
[t]Reference [8].

where volume changes on mixing, which are typically only 1–2 % for most mixtures, have been ignored. In Eq. (24) for $i=L$ and H,

$$\eta_i=\frac{\varepsilon_i-1}{\varepsilon_i+2}\ , \tag{25}$$

ε_i is the optical dielectric constant of pure liquid i and

$$\eta(z,t)=\frac{\varepsilon(z,t)-1}{\varepsilon(z,t)+2}\ . \tag{26}$$

If we invert Eq. (24) and subtract off the $z\rightarrow+\infty$ result we obtain

$$\varphi_L(z,t)-\varphi_L(+\infty,t)=\frac{\eta(z,t)-\eta(+\infty,t)}{\eta_L-\eta_H}\ . \tag{27}$$

Applying the scaling of Eq. (2) [or Eq. (4) for group H in the one-phase region] gives

$$M_-t^{\beta}\left[P_{\pm}\left[\frac{z+z_e}{\xi_{\pm}}\right]-P_{\pm}(\infty)\right] =[\eta(z,t)-\eta(+\infty,t)]/(\Delta\eta)\ , \tag{28}$$

where

$$\Delta\eta=\begin{cases}\eta_L-\eta_H & \text{for group } L\\ \eta_H-\eta_L & \text{for group } H\ .\end{cases} \tag{29}$$

If we use Eq. (26) in Eq. (28) and define the parameter

$$\Delta(z,t)=(\Delta\eta)M_-t^{\beta}\left[P_{\pm}\left[\frac{z+z_e}{\xi_{\pm}}\right]-P_{\pm}(\infty)\right]\ , \tag{30}$$

then we obtain the optical dielectric profile

$$\varepsilon(z,t)=\frac{1+2[\Delta(z,t)+\eta(+\infty,t)]}{1-[\Delta(z,t)+\eta(+\infty,t)]},\quad z\geq 0\ . \tag{31}$$

The parameter $\Delta(z,t)$ is small because $\Delta\eta$ and t^{β} are small. It will be used in a power series expansion in Appendix A. The maximum value occurs at $z=0$ and $t=0$, which can be seen by applying the asymptotic form of Eq. (8). In this limit $m(z,t)$ is independent of t and

$$\Delta_{\max}=(\Delta\eta)M_-c_{\pm}(\xi_{0\pm}/z_e)^{\beta/\nu} \tag{32}$$

is the maximum magnitude of $\Delta(z,t)$. Values for $\Delta_{\max}$ for each of the eight samples are given in Table I.

To model the optical dielectric profile $\varepsilon(z,t)$, both the critical profile of Eq. (31) and the noncritical liquid-vapor profile must be included. The noncritical profile must model the variation of the total number density of particles from its effectively zero value in the bulk vapor to the much denser bulk liquid value. This profile cannot be modeled accurately with zero adjustable parameters. Previous analyses and experiments [6,15] have found it to be only a few molecular layers thick, while the critical profile, which is scaled by the correlation length $\xi_{\pm}$, is 10–100 molecular layers thick for the reduced temperature ranges analyzed in this paper. For this reason our model will confine the noncritical profile to the vapor side ($z<0$) of the surface and neglect any perturbation that it could have on the critical profile on the liquid side ($z>0$). Near the surface in the liquid, where the power-law asymptotic form of Eq. (8) holds, the volume fraction $\varphi_L(z,t)$ is independent of t. We thus assume that the noncritical profile on the vapor side of the surface has negligible t dependence.

The approximation of Eq. (22) is equivalent to assuming that the surface is pure L (H) for group L (group H). If this assumption is valid, the noncritical profile for $z<0$ should be approximately the same as the liquid-vapor profile of the pure L (H) liquid. Thus our model will assume that for $z<0$, $\varepsilon(z)$ is the profile of the pure liquid L (H). The mean-field profile for the liquid-vapor surface of pure component i is

$$\varepsilon(z)=1+\frac{\varepsilon_i-1}{1+\exp(-z/\xi_V)} . \quad (33)$$

The noncritical vapor correlation length ξ_V scales the thickness of the noncritical profile and is typically 1–2 Å. The profile in Eq. (33) will be modified so that it will be confined to the vapor side ($z<0$) of the surface and will satisfy the condition of continuity of $\varepsilon(z)$ at $z=0$. To accomplish this we shift the noncritical profile left by z_e with the transformation $z\rightarrow z+z_e$ and change the numerator on the right-hand side of Eq. (33) so that $\varepsilon(0)=\varepsilon_i$ is satisfied. This provides the profile to be used in our analysis,

$$\varepsilon(z)=1+\frac{(\varepsilon_i-1)[1+\exp(-z_e/\xi_V)]}{1+\exp[-(z+z_e)/\xi_V]}, \quad z\leq 0 . \quad (34)$$

In Sec. IV ellipsometric measurements of the liquid-vapor surface of pure component i will be used to fix ξ_V. This leaves the noncritical profile of Eq. (34) with zero adjustable parameters.

Figure 3 shows the optical dielectric profile of Eqs. (31) and (34) for the mixtures NH and LW in the one-phase region at $t=0.01$. Although our model provides continuity of $\varepsilon(z)$ at $z=0$, it does not provide continuity of the first derivative $d\varepsilon/dz$. This discontinuity is much larger for LW, IW, and PD, where the component with the higher optical dielectric constant is preferentially adsorbed. The results of our experimental analysis in Sec. V do not seem to be significantly better or worse for these three mixtures than for the other five mixtures.

The primary purpose of this paper is to test the critical profile. We therefore proceed in Sec. IV with the strategy of making our analysis of the experimental data minimally sensitive to the specific form assumed for the noncritical profile. As a consequence, the analysis does not stringently test the accuracy of Eq. (34) and any inaccuracy in Eq. (34) should only add a small error to our conclusions for the critical profile.

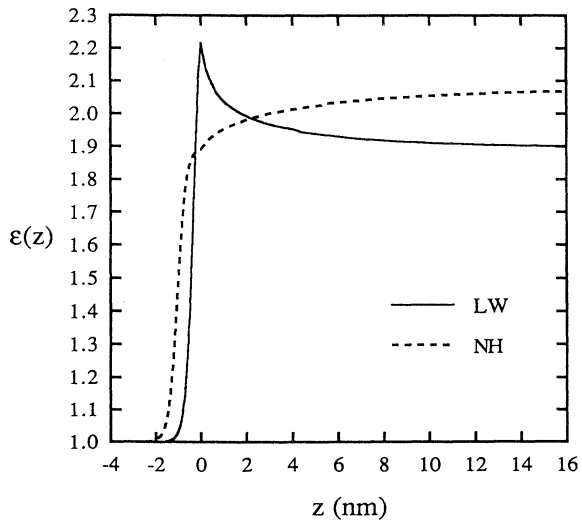

FIG. 3. Plots of the model optical dielectric surface profile $\varepsilon(z)$ as a function of z, the depth into the liquid-vapor surface. The profile is shown for the mixtures NH and LW, as labeled in the graph.

IV. ELLIPSOMETRY

Phase-modulated ellipsometry [20] is a particularly effective method for probing the order-parameter profile. A procedure established by Beaglehole [21] is to monitor the coefficient of ellipticity at the Brewster angle, defined by

$$\bar{\rho}=\mathrm{Im}\left[\frac{r_p}{r_s}\right]_{\theta_B} , \quad (35)$$

where r_p and r_s are the complex reflection amplitudes for the two independent polarizations. For thin profiles (compared with the wavelength of light $\lambda=633$ nm) the signal is described by the Drude equation [22]

$$\bar{\rho}(t)=-\frac{\pi}{\lambda}\frac{\sqrt{\varepsilon(+\infty,t)+\varepsilon(-\infty,t)}}{\varepsilon(+\infty,t)-\varepsilon(-\infty,t)} \times\int_{-\infty}^{+\infty}\frac{[\varepsilon(z,t)-\varepsilon(+\infty,t)][\varepsilon(z,t)-\varepsilon(-\infty,t)]}{\varepsilon(z,t)}dz . \quad (36)$$

The Drude equation is only valid for surface profile thicknesses that are thin compared to λ. Since z is scaled by ξ in Eq. (2), this corresponds to $\xi\ll\lambda$, which occurs far from T_c. For thicker profiles (smaller reduced temperatures), Maxwell's equations have to be solved numerically [6,23,24].

The spatial separation of the critical and noncritical profiles in our model implies that

$$\bar{\rho}=\bar{\rho}_{\mathrm{NC}}+\bar{\rho}_C , \quad (37)$$

where the noncritical part ($\bar{\rho}_{\mathrm{NC}}$) is the integral from $-\infty$ to 0 and the critical part ($\bar{\rho}_C$) is the integral from 0 to $+\infty$. The derivations of $\bar{\rho}_C$ and $\bar{\rho}_{\mathrm{NC}}$ are provided in Appendixes A and B. In the calculation of $\bar{\rho}_C$, Eq. (31) is used for $\varepsilon(z,t)$ and $\varepsilon(+\infty,t)$ in Eq. (36), while $\varepsilon(-\infty,t)=1$ for the bulk vapor phase. Equation (A5) gives the final result.

As discussed in Sec. III, the noncritical profile is assumed to be approximately the same as the liquid-vapor profile of the pure liquid L (H) for group L (H) on the vapor side ($z<0$). This enables $\bar{\rho}_{\mathrm{NC}}$ to be expressed in terms of $\bar{\rho}_{\mathrm{pure}}$, the ellipsometric measurement of the liquid-vapor surface of pure L (H). The result is given in Eq. (B6).

Using Eqs. (A5) and (B6) in Eq. (37) we obtain

$$\bar{\rho}=\bar{\rho}_{\mathrm{BG}}-\frac{\pi}{\lambda}f_\varepsilon(t)(\Delta\eta)M_-\xi_{0\pm}\left[\int P_\pm\right]t^{\beta-\nu} , \quad (38)$$

$$\bar{\rho}_{\mathrm{BG}}=\left[\frac{\varepsilon(+\infty,t)+1}{\varepsilon_i+1}\right]^{1/2}\frac{\varepsilon_i-1}{\varepsilon(+\infty,t)-1} \times[1+R_V(t)]\bar{\rho}_{\mathrm{pure}} -\frac{\pi}{\lambda}f_\varepsilon(t)(\Delta\eta)M_-\xi_{0\pm}[I_1(t)+I_2(t)] , \quad (39)$$

where ε_i is the optical dielectric constant of the preferen-

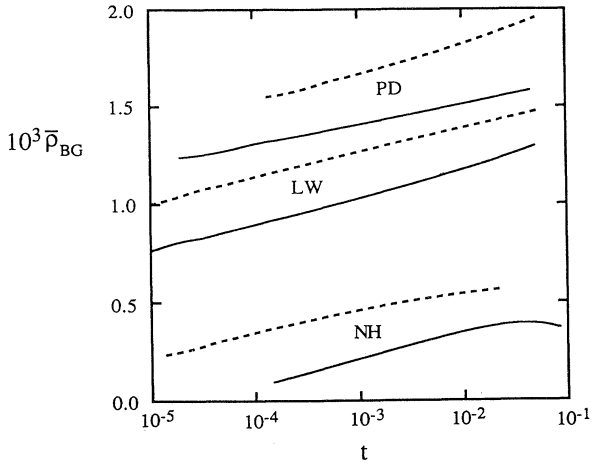

FIG. 4. Graph of the background term $\bar{\rho}_{BG}$ as a function of reduced temperature. $\bar{\rho}_{BG}$ is shown for the mixtures PD, LW, and NH as labeled, with the two-phase curve represented by the dashed lines above the label and the one-phase curve by the solid lines below. For each mixture $\bar{\rho}_{BG}$ has been calculated using Eq. (39), with the fitted $\bar{\rho}_{pure}$ values from Table IV.

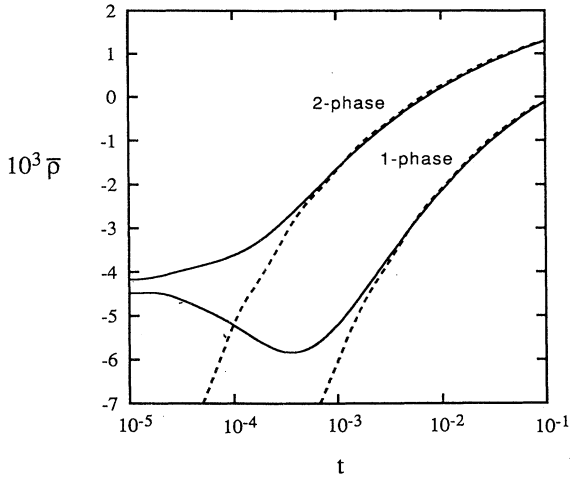

FIG. 5. Graph showing two independent calculations of $\bar{\rho}$ versus reduced temperature for the mixture LW. The solid line represents the numerical integration of Maxwell's equations for the one-phase and the two-phase regions, which is expected to be accurate over the entire range of t. The dashed lines represent Eqs. (38) and (39), which are accurate far from T_c only. From the graph we conclude that Eq. (38) is accurate for $t>0.004$ for the one-phase region and for $t>0.0008$ for the two-phase region.

tially adsorbed pure component. The quantities $R_V(t)$, $f_\varepsilon(t)$, $I_1(t)$, and $I_2(t)$, defined in Eqs. (B7), (A4), (A8), and (A9), have a weak nondiverging dependence on t. Therefore the background term $\bar{\rho}_{BG}$ has a weak nondiverging dependence on t, while the second term in Eq. (38) diverges as $t^{\beta-\nu}$. In Sec. VI Eqs. (38) and (39) will be applied to the ellipsometric data, where $\xi_{0\pm}M_-\int P_\pm$, $\beta-\nu$, and $\bar{\rho}_{pure}$ are statistically fitted. Equation (38) is dominated by the diverging $t^{\beta-\nu}$ term, allowing $\int P_\pm$ and $\beta-\nu$ to be determined with reasonable precision. Also, as discussed in Appendix B, fitting $\bar{\rho}_{pure}$ in Eq. (39) prevents the inaccuracy of the model noncritical profile of Eq. (34) from causing significant error to the fitted $\int P_\pm$ and $\beta-\nu$ values.

Previously [15,17] $\bar{\rho}_{BG}$ was treated as a constant and part of the prefactor to $\int P_\pm t^{\beta-\nu}$ was assumed to be an unknown constant. This allowed the experimental determination of R_{MA}, but not the individual integrals $\int P_\pm$. The fitted $\bar{\rho}_{BG}$ values ranged from 0.1×10^{-3} to 1.8×10^{-3} for the five mixtures studied. The specific values obtained were not quantitatively understood. In Fig. 4 $\bar{\rho}_{BG}$ is graphed using Eq. (39) for three mixtures, with the one-phase result represented by solid lines and the two-phase result by dashed lines. The values used for $\bar{\rho}_{pure}$ are the fitted results given in Table IV and discussed in Sec. V. Over the range of reduced temperatures for which Eqs. (38) and (39) are valid, the variation of $\bar{\rho}_{BG}$ is typically less than 10^{-4}. Thus we can conclude that if one is only interested in checking the $t^{\beta-\nu}$ scaling of ellipsometric measurements on critical adsorption in binary liquid mixtures, the simpler fitting scheme described in Ref. [15] and [17] would be adequate.

In Ref. [24] we numerically integrate Maxwell's equations with the renormalization-group or the Monte Carlo surface scaling functions $P_\pm(x)$ in order to produce theoretical $(\bar{\rho},t)$ curves. The numerical integration scheme of Maxwell's equations [23] has been tested extensively against exact results and is therefore believed to be accurate over the entire range of experimentally accessible reduced temperatures. To determine the range of t over which Eqs. (38) and (39) are accurate, we graphed the Monte Carlo numerical $(\bar{\rho},t)$ curves together with Eq. (38) for each mixture. Figure 5 shows the comparison for LW, with the numerical results represented by the solid lines and Eq. (38) by the dashed lines. From these comparisons we determined that Eqs. (38) and (39) are valid over the fitting ranges stated in Table IV. In the specified reduced temperature ranges, ξ is always an order of magnitude smaller than λ.

V. EXPERIMENTAL DETAILS

Sample preparation and ellipsometric measurement procedures are discussed in Ref. [17], while graphs representing the $(\bar{\rho},t)$ experimental data for the eight liquid mixtures are provided in Refs. [8,14–17]. Analysis of the experimental data using Eqs. (38) and (39) requires measured values for ε_H, ε_L, M_-, ξ_{0+}, and $\varphi_L(+\infty,0)$ for each liquid mixture. Values and references for these quantities are provided in Table II. Values for $\varepsilon(+\infty,t)=n^2$ were determined from index of refraction measurements (Table III) when available or else calculated from the coexistence curve using the Clausius-Mossotti equation (24).

The most reliable method of checking that a sample has been mixed at the critical volume fraction is to verify that after a quench from the one-phase to the two-phase

TABLE III. Bulk index of refraction as a function of reduced temperature for the one-phase and the upper two-phase regions.

Mixture	One-phase region $n(t)$	Reference
AC	$1.490-0.157t-0.007t^{1-\alpha}$	[29]
IW	$1.3609-0.0738t$	[19]
LW	$1.3772+0.08t$	[42]
NH	$1.444-0.164t+0.0116t^{1-\alpha}$	[36]
PD	1.39	[43]
CM	$1.380-0.1615t$	[39]
HA	$1.388-0.135t$	[43]
Sch	$1.333-0.206t$	[8]

Mixture	Upper two-phase region $n(t)$	Reference
AC	$1.490+0.157t-2(0.007)t^{1-\alpha}-0.157t^{\beta}$	[29]
IW	$1.3609+0.0738t+0.048t^{\beta}$	[19]
LW	$1.3772-0.08t+0.144t^{\beta}$	[34,42]
NH	$1.444+0.164t+2(0.0116)t^{1-\alpha}-0.14t^{\beta}(1+0.4t^{\Delta})$	[36]
PD	$1.39-0.0827t^{\beta}$	[43]

region the meniscus forms in the middle of the sample cell near the critical temperature in the two-phase region. Of the seven mixtures we have prepared, this was verified only for LW, NH, and PD. The other samples were mixed at concentrations stated to be critical in the literature, without verification of criticality. In Ref. [17] it was shown that a sample of 1.3% below the critical mass fraction gave significantly different ellipsometric measurements in the one-phase region, but the two-phase data were unaffected because the upper phase retains the correct concentration. For this reason we have more confidence in the one-phase results for LW, NH, and PD than for the other mixtures. The one- and the two-phase ellipsometric data for these three mixtures are provided in Appendix C.

VI. ANALYSIS AND RESULTS

Nonlinear least-squares regression [25] was used to fit the $(\bar{\rho},t)$ data to Eqs. (38) and (39), where the Monte Carlo results have been used to estimate $I_1(t)$ and $I_2(t)$ in Eq. (39), and Eq. (34) has been used in estimating $R_V(t)$ in Eq. (39). The results are given for each mixture in Table IV. The reduced temperature range over which the data were fitted was restricted to the range over which Eqs. (38) and (39) are valid, as discussed in Sec. IV and shown in Fig. 5. The reduced temperature range was generally wider for the two-phase fit than the one-phase fit. Initially $\bar{\rho}_{\text{pure}}$, $\xi_{0\pm}M_-\int P_\pm$, and $\beta-\nu$ were fitted for each mixture, with the exception of CM and Sch, which contained too few data points to justify a three parameter fit. We obtain $\beta-\nu=-0.302\pm0.005$, in excellent agreement with the theoretical value of -0.304 ($\beta=0.328$ and $\nu=0.632$). Next $\bar{\rho}_{\text{pure}}$ and $\xi_{0\pm}M_-\int P_\pm$ were fitted with $\beta-\nu=-0.304$ fixed at the theoretical value. This allowed $\bar{\rho}_{\text{pure}}$ and $\xi_{0\pm}M_-\int P_\pm$ to be determined with greater precision. Figure 6(a) shows the experimental data for LW (open squares) and the fit to Eq. (38) (solid lines). Figure 6(b) shows the ratio of the residuals $\bar{\rho}_{\text{expt}}-\bar{\rho}_{\text{fit}}$ to the reproducibility of the individual $\bar{\rho}$ measurements $\Delta\bar{\rho}=5\times10^{-5}$ for the mixtures LW, NH, and PD in the one- and the two-phase regions. Figure 6(b) shows that most of the experimental data fall within two standard deviations of the fitted value and no systematic variation of the residuals as a function of the reduced temperature is detectable.

In Table IV both the fitted and the measured $\bar{\rho}_{\text{pure}}$ values are given. The agreement is reasonable, except for the one-phase fits of AC, IW, and PD. Since the agreement is good in the two-phase region, it seems unlikely that these one-phase discrepancies are caused by an inaccuracy in the model noncritical profile of Eq. (34). Although there are a number of possible causes, we cannot make a sound conclusion on the source of these three discrepancies at this time.

To calculate the $\int P_\pm$ values stated in Table IV, the values for $\xi_{0\pm}$ and M_- from Table II were divided out of the fitted $\xi_{0\pm}M_-\int P_\pm$ values, where Eq. (3) was used to determine ξ_{0-} in the two-phase region. The quoted uncertainties for $\int P_\pm$ in Table IV were calculated from the uncertainties in $\xi_{0\pm}M_-\int P_\pm$, $\xi_{0\pm}$, and M_-. The error contributions to $\int P_\pm$ from $\varepsilon(+\infty,t)$, ε_H, ε_L, and $\varphi_L(+\infty,0)$ have been ignored because they are determined with much greater precision. To calculate the R_{MA} values quoted in Table IV, the fitted values for $\xi_{0+}M_-\int P_+$ and $\xi_{0-}M_-\int P_-$ are divided, so that R_{MA} has the advantage of being independent of M_- and ξ_{0+} [where Eq. (3) was used].

For the eight mixtures, the experimental means for $\int P_+$, $\int P_-$, and R_{MA} are 1.84 ± 0.08, 1.63 ± 0.08, and 1.08 ± 0.08, respectively, stated with one standard deviation errors. In calculating each mean and error the individual $\int P_\pm$ and R_{MA} values were weighted by their errors σ_i [25]. The quoted result is $\bar{x}_w\pm s_w$, where

$$\bar{x}_w = \langle x_i \rangle_w = \frac{\sum_{i=1}^{N} (x_i/\sigma_i^2)}{\sum_{i=1}^{N} (1/\sigma_i^2)} , \tag{40}$$

$$s_w^2 = \frac{\langle (x_i - \bar{x}_w)^2 \rangle_w}{N-1} = \frac{\sum_{i=1}^{N} [(x_i - \bar{x}_w)^2/\sigma_i^2]}{(N-1)\sum_{i=1}^{N} (1/\sigma_i^2)} . \tag{41}$$

As discussed in Sec. V, criticality was verified for the mixtures LW, NH, and PD only. The error weighted means for these three mixtures are $\int P_+ = 1.80 \pm 0.11$, $\int P_- = 1.61 \pm 0.04$, and $R_{MA} = 1.15 \pm 0.04$, where the errors represent one standard deviation. We prefer these results, although they differ only marginally from the error-weighted means quoted above for all mixtures.

In Ref. [24] we numerically integrate Maxwell's equations with the renormalization-group or the Monte Carlo surface scaling functions $P_\pm(x)$ in order to produce theoretical $(\bar{\rho}, t)$ curves. To check for systematic errors in our analysis, we fitted Eqs. (38) and (39) to the Monte Carlo $(\bar{\rho}, t)$ data for all eight mixtures and obtained means of $\int P_+ = 2.11$, $\int P_- = 1.97$, and $R_{MA} = 1.07$. These results for $\int P_+$, $\int P_-$, and R_{MA} are, respectively, 3.3%, 0%, and 3.9%, low compared with the exact results obtained by direct integration of the Monte Carlo

TABLE IV. Nonlinear least-squares fit of Eqs. (38) and (39) to ellipsometric data far from T_c. (Quoted errors are one standard deviation.)

Mixture	Phase	Reduced temperature range	$\beta-\nu$[a]	Fitted $\bar{\rho}_{\text{pure}}$ (10^{-3})	Measured $\bar{\rho}_{\text{pure}}$ (10^{-3})[b]	$\int P_\pm$	R_{MA}[c]	χ^2
AC	1	$0.002 < t < 0.02$	-0.300 ± 0.010	1.78 ± 0.08	1.09 ± 0.05(C)	1.78 ± 0.18	0.88 ± 0.03	2.5
AC	1	$0.002 < t < 0.02$	-0.304	1.80 ± 0.05	(1.22 ± 0.05)[d]	1.72 ± 0.11		2.4
AC	2	$0.0009 < t < 0.03$	-0.305 ± 0.013	0.99 ± 0.09		1.94 ± 0.27		0.33
AC	2	$0.0009 < t < 0.03$	-0.304	0.98 ± 0.04		1.96 ± 0.12		0.32
IW	1	$0.006 < t$	-0.300 ± 0.12	1.6 ± 0.9	0.90 ± 0.05(I)	2.6 ± 2	1.75 ± 0.12	0.15
IW	1	$0.006 < t$	-0.304	1.56 ± 0.06		2.47 ± 0.15		0.14
IW	2	$0.0015 < t$	-0.306 ± 0.016	0.90 ± 0.05		1.39 ± 0.18		0.72
IW	2	$0.0015 < t$	-0.304	0.90 ± 0.06		1.41 ± 0.12		0.68
LW	1	$0.004 < t$	-0.305 ± 0.011	1.13 ± 0.23	1.06 ± 0.05(L)	1.80 ± 0.18	1.17 ± 0.02	0.74
LW	1	$0.004 < t$	-0.304	1.15 ± 0.10		1.82 ± 0.10		0.70
LW	2	$0.0008 < 1$	-0.305 ± 0.012	0.96 ± 0.08		1.54 ± 0.18		0.77
LW	2	$0.0008 < t$	-0.304	0.97 ± 0.03		1.56 ± 0.08		0.73
NH	1	$0.005 < t < 0.02$	-0.303 ± 0.027	1.37 ± 0.21	1.03 ± 0.05(H)	1.64 ± 0.35	1.03 ± 0.04	2.7
NH	1	$0.005 < t < 0.02$	-0.304	1.38 ± 0.07		1.63 ± 0.10		2.6
NH	2	$0.0015 < t$	-0.297 ± 0.013	0.99 ± 0.08		1.69 ± 0.21		3.2
NH	2	$0.0015 < t$	-0.304	1.03 ± 0.04		1.59 ± 0.09		3.1
PD	1	$0.01 < t$	-0.307 ± 0.050	2 ± 1	1.10 ± 0.05(P)	1.99 ± 0.72	1.20 ± 0.05	1.1
PD	1	$0.01 < t$	-0.304	2.02 ± 0.24		2.04 ± 0.13		0.95
PD	2	$0.002 < t$	-0.306 ± 0.006	1.18 ± 0.06		1.67 ± 0.11		1.6
PD	2	$0.002 < t$	-0.304	1.20 ± 0.05		1.70 ± 0.09		1.5
CM	1	$0.004 < t$	-0.304	0.61 ± 0.18	0.74 ± 0.05(M) (0.66 ± 0.05)[d]	1.91 ± 0.18		0.14
HA	1	$0.002 < t$	-0.306 ± 0.007	0.83 ± 0.03	0.78 ± 0.05(A)	1.91 ± 0.14		0.87
HA	1	$0.002 < t$	-0.304	0.82 ± 0.03		1.95 ± 0.11		0.83
Sch	1	$0.003 < 1$	-0.304	1.09 ± 0.06	(0.86,0.87,1.02)[e] (C_7F_{14})	1.65 ± 0.10		0.39

[a]The value of -0.304 implies that $\beta-\nu$ has been fixed at this value.
[b]Measured at room temperature for this publication, unless otherwise noted. "(C)" indicates that the value was measured on pure cyclohexane, "(I)" indicates isobutyric acid, etc. These are the components that are preferentially adsorbed at the surface.
[c]Calculated from the one- and two-phase fits with β-ν fixed.
[d]From Ref. [8], at $T = 25$ °C.
[e]From Ref. [8], at 26, 40, and 51 °C, respectively.

functions $P_{\pm}(x)$ in Sec. II. This suggests that the fitted experimental $\int P_+$ and R_{MA} values are also slightly low. We thus add these systematic errors to the experimental means of our three best mixtures to obtain our final experimental results

$$\int P_+ = 1.86 \pm 0.11 \ , \tag{42}$$

$$\int P_- = 1.61 \pm 0.04 \ , \tag{43}$$

$$R_{MA} = 1.19 \pm 0.04 \ . \tag{44}$$

In Figs. 7(a)–7(c) the experimental $\int P_{\pm}$ and R_{MA} values are represented by open squares with error bars of

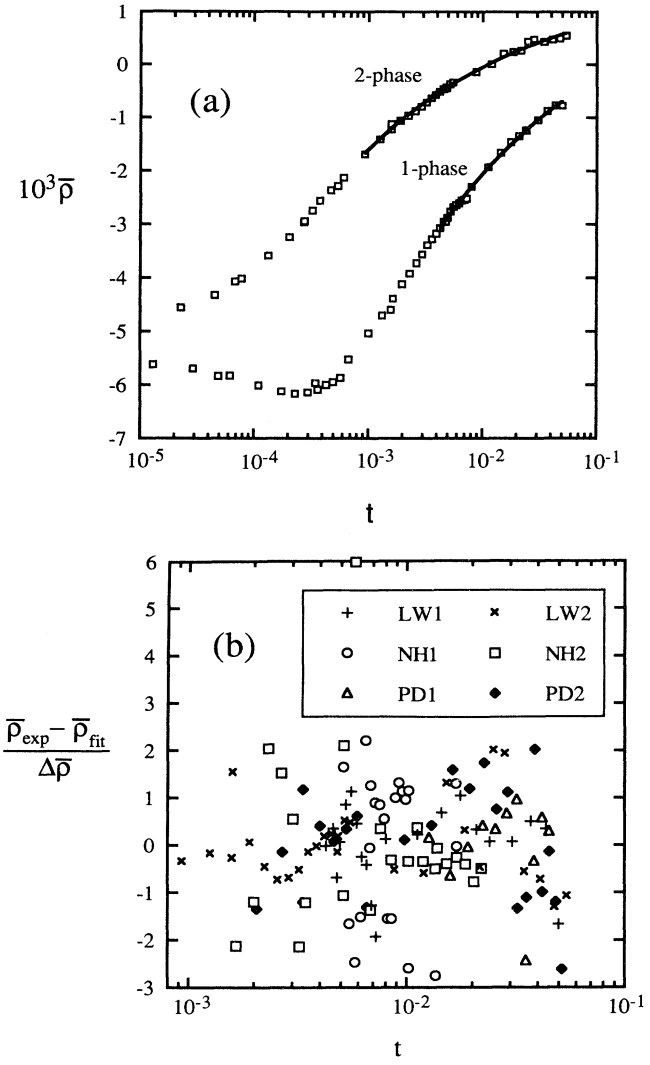

FIG. 6. (a) Ellipsometric data for the mixture LW (open squares) in the one-phase and the two-phase regions and the fit of the data to Eqs. (38) and (39) (solid lines). (b) Ratio of the residual $\bar{\rho}_{\text{expt}} - \bar{\rho}_{\text{fit}}$ to the reproducibility of the individual $\bar{\rho}$ measurements, $\Delta\bar{\rho} = 5 \times 10^{-5}$ versus reduced temperature. $\bar{\rho}_{\text{expt}}$ is the experimental $\bar{\rho}$ data, while $\bar{\rho}_{\text{fit}}$ is the function fitted to the data using Eqs. (38) and (39). The key indicates both mixture and phase.

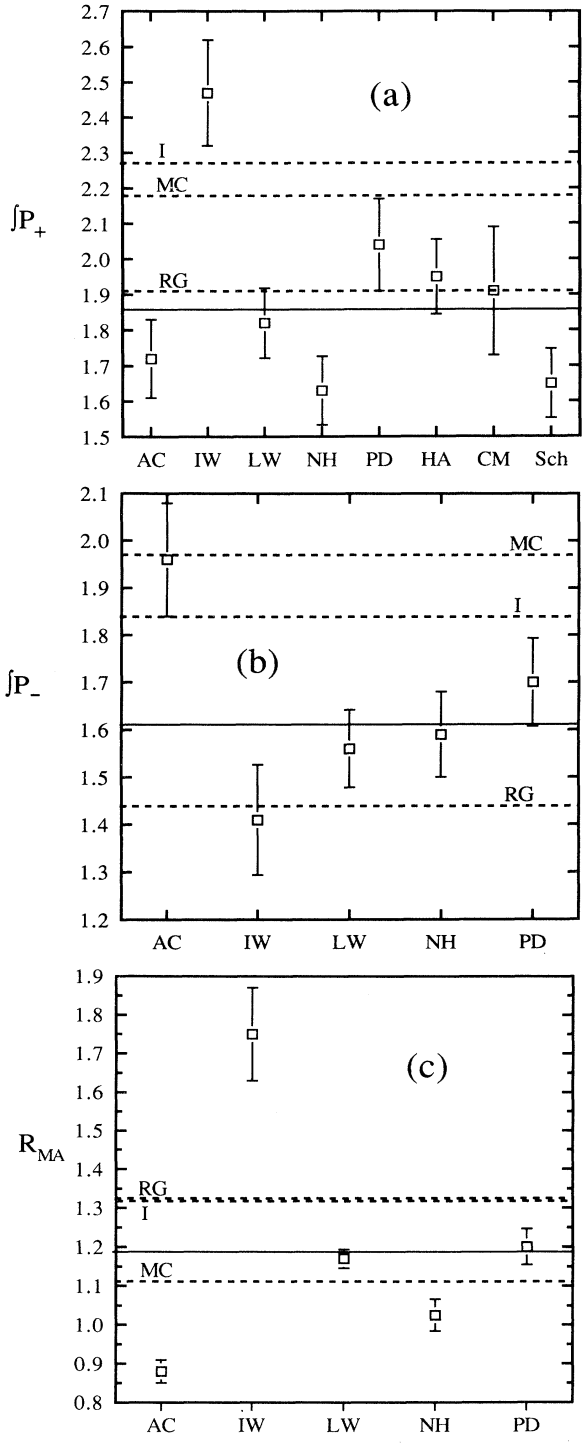

FIG. 7. Plots representing (a) $\int P_+$, (b) $\int P_-$, and (c) R_{MA}. The squares with one standard deviation error bars represent the values for each mixture determined by fits of Eqs. (38) and (39) to the experimental data using nonlinear least-squares regression. The solid lines show the experimental error-weighted mean of the three most reliable samples LW, NH, and PD, shifted to compensate for small systematic errors. The dashed lines show the theoretical renormalization-group Monte Carlo, and interpolation values, labeled by RG, MC, and *I*, respectively.

one standard deviation. The solid lines represent the experimental results of Eqs. (42)–(44). The dashed lines labeled RG and MC represent the theoretical $\int P_{\pm}$ and R_{MA} values calculated directly from the renormalization-group and Monte Carlo profiles, respectively, as discussed in Sec. II. The dashed lines labeled I represent the theoretical values obtained from the interpolation study. Except for the one-phase result of IW and the two-phase result of AC, all the experimental $\int P_{\pm}$ values are within two standard deviations of the experimental results of Eqs. (42) and (43). The R_{MA} values for the three most reliable mixtures LW, NH, and PD are also in reasonable agreement. We hope to clear up the discrepant $\int P_{\pm}$ and R_{MA} values by remeasuring AC and IW samples for which criticality has been verified in a future paper [26].

Finally, we have also examined the effects of slight changes in $I_1(t)$, $I_2(t)$, and $R_V(t)$ on the experimental values for $\int P_{\pm}$ and R_{MA}. The experimental $(\bar{\rho},t)$ data were refitted to Eqs. (38) and (39) with the Monte Carlo results for $I_1(t)$, $I_2(t)$, and z_e [which affects $R_V(t)$ in Eq. (B7)] replaced by the renormalization-group results. We found that $\int P_{\pm}$ and R_{MA} are changed by less than 1%.

VII. SUMMARY AND CONCLUSIONS

We have presented a method of analyzing ellipsometric data on critical adsorption in binary liquid mixtures. Using the data far from T_c, our analysis determines the universal integrals $\int P_{\pm}$ defined in Eqs. (10) and (11). We have presented evidence that, provided M_- and ξ_{0+} are measured accurately for the mixture, the method determines $\int P_-$ from the two-phase data very accurately, while the fitted value for $\int P_+$ from the one-phase data and the result for R_{MA} are systematically low by approximately 3–4%. The cause of the systematic error is not understood.

We have applied this analysis to existing data on eight critical binary liquid mixtures [8,14–17]. The mean values from the three most reliable data sets, taken on the mixtures LW, NH, and PD, are $\int P_+ = 1.86 \pm 0.11$, $\int P_- = 1.61 \pm 0.04$, and $R_{MA} = 1.19 \pm 0.04$ for the ratio defined in Eq. (9). The systematic errors have been added to the mean values and the quoted errors represent one standard deviation. While errors in the experimentally determined values of M_- and ξ_{0+} for each mixture cause errors in the experimental $\int P_{\pm}$ values, the determination of the ratio R_{MA} is independent of these parameters.

In Table V the three sets of theoretical values for the universal quantities $\int P_{\pm}$ and R_{MA} are compared with our experimental values. Our experimental result for $\int P_+$ agrees well with the renormalization-group result but is more than three standard deviations lower than the interpolation value. Our experimental $\int P_-$ result is significantly higher than the renormalization-group value and significantly lower than the Monte Carlo value. The experimental R_{MA} value is in reasonable agreement with the Monte Carlo value, but is significantly lower than the renormalization-group and interpolation results. In summary, although we now possess a far better qualitative understanding of the critical adsorption amplitudes, none of the three theoretical studies are in consistent quantitative agreement with our experimental results.

In all previous experimental studies of critical adsorption the contributions to $\bar{\rho}$ from capillary wave fluctuations have been ignored, probably because these contributions are expected to be small. The capillary wave contributions scale as σ^{-1}, where σ is the surface tension. They provide a significant contribution to $\bar{\rho}$ for the critical interface [27], where σ is small. We will consider this contribution in a future paper to see if it can resolve the discrepancies between theory and experiment for critical adsorption.

We hope that this experimental study will stimulate further theoretical work on critical adsorption. We note a number of theoretical issues which still have to be resolved before we can be completely satisfied with the theoretical surface scaling functions $P_{\pm}(x)$. At present the uncertainties on the estimates of $\int P_{\pm}$ and R_{MA} for the renormalization-group calculations [10] and Monte Carlo simulations [11] are not known, while the uncertainties on $\int P_{\pm}$ for the interpolation theory are rather large. The Monte Carlo simulations display an oscillation in $P_-(x)-1$ rather than a purely exponential decay for large x, as discussed in Sec. II and displayed in Fig. 2(b). Equations (3) and (23) imply that the ratio c_+/c_- has the universal value 0.71. While the Monte Carlo results yield the value 0.71 for this ratio, the interpolation and renormalization-group results give 0.76±0.05 and 0.64, respectively. Finally, we believe that in the two-phase region desorption of the lighter component L from the upper liquid-vapor surface needs to be considered

TABLE V. Comparison of the experimental mean with the existing theoretical values for the universal critical adsorption parameters $\int P_{\pm}$ and R_{MA} defined in Eqs. (9)–(11).

	$\int P_+$	$\int P_-$	R_{MA}
Experimental mean[a]	1.86±0.11	1.61±0.04	1.19±0.04
Renormalization group[b]	1.91	1.44	1.33
Monte Carlo[c]	2.18	1.97	1.11
Interpolation[d]	2.27±0.33	1.84±0.33	1.32±0.07

[a]Determined in this publication.
[b]Reference [10].
[c]Reference [11].
[d]Reference [13].

more carefully theoretically [2].

It appears that further work is necessary in order to resolve the discrepancies between experiment, computer simulation, and theory, before an accurate quantitative description of critical adsorption can be achieved at noncritical surfaces.

ACKNOWLEDGMENTS

We wish to thank Professor H. W. Diehl, Martin Smock, and Professor D. P. Landau for supplying numerical values and asymptotic forms for the theoretical surface scaling functions from the renormalization-group study and Monte Carlo simulation. We also thank G. Flöter and Professor S. Dietrich for providing us with a copy of their work before publication. This work was supported by the National Science Foundation through Grant No. DMR-9208123.

APPENDIX A: DERIVATION OF $\bar{\rho}_C$

In Eqs. (36) and (37), $\bar{\rho}_C$ is defined as the integral over the critical adsorption profile in the liquid, from 0 to $+\infty$. Setting $\varepsilon(-\infty,t)=1$ for the bulk vapor phase and using Eq. (31) for $\varepsilon(z,t)$ in Eq. (36) gives after simplification

$$\bar{\rho}_C=-\frac{\pi}{\lambda}\frac{\sqrt{\varepsilon(+\infty,t)+1}[\varepsilon(+\infty,t)+2]^2}{3\varepsilon(+\infty,t)}\int_0^{+\infty}\frac{\Delta(z,t)\left[1+\dfrac{\Delta(z,t)}{\eta(+\infty,t)}\right]}{\left[1-\dfrac{\Delta(z,t)}{1-\eta(+\infty,t)}\right]\left[1+\dfrac{2\Delta(z,t)}{1+2\eta(+\infty,t)}\right]}dz\ . \tag{A1}$$

No approximations have been made here, beyond the approximations inherent in Eq. (31) and (36). A binomial expansion gives

$$\frac{1}{\left[1-\dfrac{\Delta(z,t)}{1-\eta(+\infty,t)}\right]\left[1+\dfrac{2\Delta(z,t)}{1+2\eta(+\infty,t)}\right]}=1-\frac{[1-4\eta(+\infty,t)]\Delta(z,t)}{[1-\eta(+\infty,t)][1+2\eta(+\infty,t)]}+O[\Delta^2(z,t)]\ , \tag{A2}$$

where $O[\Delta^2(z,t)]$ represents terms of order $[\Delta(z,t)]^2$ and higher. Values of the first-order correction in (A2) at $z=0$ and $t=0$ are given for the eight liquid mixtures in Table I. Since $\eta(+\infty,t)\cong\frac{1}{4}$ in addition to $\Delta(z,t)$ being small, this correction is extremely small and will be neglected. Equation (A1) then becomes

$$\bar{\rho}_C=-\frac{\pi}{\lambda}f_\varepsilon(t)\int_0^{+\infty}\Delta(z,t)[1+\Delta(z,t)/\eta(+\infty,t)]dz\ , \tag{A3}$$

where

$$f_\varepsilon(t)=\frac{\sqrt{\varepsilon(+\infty,t)+1}[\varepsilon(+\infty,t)+2]^2}{3\varepsilon(+\infty,t)}\ . \tag{A4}$$

Now using definition (30) and the substitution $x=(z+z_e)/\xi_\pm$, Eq. (A3) becomes

$$\bar{\rho}_C=-\frac{\pi}{\lambda}f_\varepsilon(t)(\Delta\eta)M_-\xi_{0\pm}\times\left[I_1(t)+I_2(t)+\left[\int P_\pm\right]t^{\beta-\nu}\right]\ , \tag{A5}$$

where

$$I_1(t)=\frac{(\Delta\eta)M_-}{\eta(+\infty,t)}\int_{z_e/\xi_\pm}^{+\infty}[P_\pm(x)-P_\pm(\infty)]^2dx\ t^{2\beta-\nu}\ , \tag{A6}$$

$$I_2(t)=-\int_0^{z_e/\xi_\pm}[P_\pm(x)-P_\pm(\infty)]dx\ t^{\beta-\nu}\ , \tag{A7}$$

and $\int P_\pm$ are defined in Eqs. (10) and (11). $I_1(t)$ and $I_2(t)$ are small compared with the third term in Eq. (A5). Rather than neglecting $I_1(t)$ and $I_2(t)$ entirely in Eq. (A5), we approximate their behavior by assuming that the Monte Carlo functions for $P_\pm(x)$ [11] are sufficiently close to reality and can be used in Eqs. (A6) and (A7). This assumption is tested in Sec. VI.

The asymptotic form of Eq. (8) can be used in Eq. (A7) to give

$$I_2(t)=P_\pm(\infty)(z_e/\xi_{0\pm})t^\beta-\frac{c_\pm}{1-\beta/\nu}(z_e/\xi_{0\pm})^{1-\beta/\nu}\ . \tag{A8}$$

The integral I_1 is determined by using the asymptotic form of Eq. (8) from $z_e/\xi_\pm$ to x_1, numerical integration from x_1 to x_2, and the asymptotic form of Eq. (7) from x_2 to $+\infty$,

$$I_1(t)=\frac{(\Delta\eta)M_-}{\eta(+\infty,t)}\left\{\frac{c_\pm^2}{2\beta/\nu-1}(\xi_{0\pm}/z_e)^{2\beta/\nu-1}+\left[x_1P_\pm(\infty)+I'_\pm+\tfrac{1}{2}(P_{\infty,\pm})^2\exp(-2x_2)-\frac{c_\pm^2}{(2\beta/\nu-1)x_1^{2\beta/\nu-1}}-\frac{2c_\pm x_1^{1-\beta/\nu}P_\pm(\infty)}{1-\beta/\nu}\right]t^{2\beta-\nu}+\frac{2c_\pm}{1-\beta/\nu}(z_e/\xi_{0\pm})^{1-\beta/\nu}P_\pm(\infty)t^\beta-(z_e/\xi_{0\pm})P_\pm(\infty)t^{2\beta}\right\}\ . \tag{A9}$$

Values for x_1 and x_2 were given for the renormalization-group and Monte Carlo functions in Sec. II. The quantity $I'_{\pm}$ appearing in Eq. (A9) is defined by

$$I'_{\pm}=\int_{x_1}^{x_2}[P_{\pm}(x)-P_{\pm}(\infty)]^2dx=\begin{cases}0.952, & +\\ 0.648, & -\end{cases} \quad \text{(A10)}$$

where the numerical values are obtained using the Monte Carlo functions $P_{\pm}(x)$. The renormalization-group scaling functions give $I'_{+}=0.398$ and $I'_{-}=0.104$.

APPENDIX B: DERIVATION OF $\bar{\rho}_{\rm NC}$

In Eq. (36) and (37), $\bar{\rho}_{\rm NC}$ is defined as the integral over the noncritical liquid-vapor profile in the vapor, from $-\infty$ to 0. Setting $\varepsilon(-\infty,t)=1$ for the bulk vapor phase,

$$\bar{\rho}_{\rm NC}=-\frac{\pi}{\lambda}\frac{\sqrt{\varepsilon(+\infty,t)+1}}{\varepsilon(+\infty,t)-1}\times\int_{-\infty}^{0}\frac{[\varepsilon(z)-\varepsilon(+\infty,t)][\varepsilon(z)-1]}{\varepsilon(z)}dz\ . \quad \text{(B1)}$$

As discussed in Sec. III, the noncritical profile will be confined to the vapor side ($z<0$) of the surface and will be assumed to be approximately the same as the liquid-vapor profile of the pure liquid L (H) for group L (group H). Under this approximation, the Drude equation (36) applied to the ellipsometric measurement of the liquid-vapor surface of pure L (H) gives

$$\bar{\rho}_{\rm pure}=-\frac{\pi}{\lambda}\frac{\sqrt{\varepsilon_i+1}}{\varepsilon_i-1}\int_{-\infty}^{0}\frac{[\varepsilon(z)-\varepsilon_i][\varepsilon(z)-1]}{\varepsilon(z)}dz\ . \quad \text{(B2)}$$

The noncritical optical dielectric profile constructed for our model is given in Eq. (34), which when used in Eq. (B2) gives

$$\bar{\rho}_{\rm pure}=-\frac{\pi}{\lambda}\sqrt{\varepsilon_i+1}[1+\exp(-z_e/\xi_V)]\xi_V\times\left\{\ln[1+\exp(z_e/\xi_V)]-\frac{\varepsilon_i}{\varepsilon_i+(\varepsilon_i-1)\exp(-z_e/\xi_V)}\times\ln\{\varepsilon_i[1+\exp(z_e/\xi_V)]\}\right\}. \quad \text{(B3)}$$

TABLE VI. Reduced temperature versus $\bar{\rho}$ data for the critical mixture LW (2,6 lutidine–water).

t	$\bar{\rho}$ (10^{-3})	t	$\bar{\rho}$ (10^{-3})	t	$\bar{\rho}$ (10^{-3})
		LW one-phase region			
4.989×10^{-2}	−0.772	5.255×10^{-3}	−2.758	1.005×10^{-3}	−5.037
4.346×10^{-2}	−0.768	4.932×10^{-3}	−2.878	6.756×10^{-4}	−5.520
3.703×10^{-2}	−0.877	4.798×10^{-3}	−2.951	5.744×10^{-4}	−5.870
3.058×10^{-2}	−1.044	4.596×10^{-3}	−2.955	4.961×10^{-4}	−5.948
2.413×10^{-2}	−1.234	4.269×10^{-3}	−3.071	4.341×10^{-4}	−6.003
2.091×10^{-2}	−1.342	3.939×10^{-3}	−3.174	3.656×10^{-4}	−6.087
1.769×10^{-2}	−1.453	3.613×10^{-3}	−3.273	3.492×10^{-4}	−5.966
1.447×10^{-2}	−1.657	3.287×10^{-3}	−3.386	3.003×10^{-4}	−6.138
1.124×10^{-2}	−1.928	2.964×10^{-3}	−3.559	2.317×10^{-4}	−6.160
8.023×10^{-3}	−2.292	2.640×10^{-3}	−3.722	1.762×10^{-4}	−6.119
7.229×10^{-3}	−2.513	2.311×10^{-3}	−3.919	1.110×10^{-4}	−6.008
6.900×10^{-3}	−2.534	1.981×10^{-3}	−4.114	6.201×10^{-5}	−5.828
6.564×10^{-3}	−2.550	1.655×10^{-3}	−4.384	4.896×10^{-5}	−5.833
6.234×10^{-3}	−2.603	1.576×10^{-3}	−4.593	2.937×10^{-5}	−5.694
5.901×10^{-3}	−2.634	1.322×10^{-3}	−4.701	1.306×10^{-5}	−5.615
5.571×10^{-3}	−2.671				
		LW two-phase region			
5.416×10^{-2}	0.551	4.821×10^{-3}	−0.444	6.103×10^{-4}	−2.124
4.768×10^{-2}	0.499	4.527×10^{-3}	−0.462	5.451×10^{-4}	−2.280
4.121×10^{-2}	0.480	4.191×10^{-3}	−0.511	4.733×10^{-4}	−2.360
3.475×10^{-2}	0.430	3.871×10^{-3}	−0.571	3.786×10^{-4}	−2.553
2.827×10^{-2}	0.482	3.551×10^{-3}	−0.631	3.264×10^{-4}	−2.741
2.500×10^{-2}	0.440	3.225×10^{-3}	−0.713	2.774×10^{-4}	−2.941
2.177×10^{-2}	0.263	2.898×10^{-3}	−0.792	2.742×10^{-4}	−2.966
1.853×10^{-2}	0.238	2.572×10^{-3}	−0.876	2.056×10^{-4}	−3.238
1.528×10^{-2}	0.208	2.242×10^{-3}	−0.961	1.338×10^{-4}	−3.585
1.204×10^{-2}	0.008	1.909×10^{-3}	−1.055	7.833×10^{-5}	−4.017
8.816×10^{-3}	−0.137	1.593×10^{-3}	−1.123	6.854×10^{-5}	−4.069
5.516×10^{-3}	−0.335	1.586×10^{-3}	−1.217	4.569×10^{-5}	−4.321
5.183×10^{-3}	−0.369	1.257×10^{-3}	−1.406	2.285×10^{-5}	−4.554
4.844×10^{-3}	−0.425	9.302×10^{-4}	−1.685		

In Table IV the values given for $\bar{\rho}_{\text{pure}}$ were measured on the liquid-vapor surface of pure component L (H) for group L (group H). For each mixture the noncritical vapor correlation length ξ_V was calculated from Eq. (B3) using the measured value of $\bar{\rho}_{\text{pure}}$. These ξ_V values are provided in Table II. Our measured value of $\bar{\rho}_{\text{pure}}$ has been used for each mixture except for Sch, where $\bar{\rho}_{\text{pure}}=0.94\times10^{-3}$ was used.

With ξ_V fixed, Eq. (34) could be applied to Eq. (B1) to give $\bar{\rho}_{\text{NC}}$ with no adjustable parameters. This, however, would make our analysis quite sensitive to the inaccuracy of our model noncritical profile. As stated in Sec. III, we want to minimize the sensitivity of our analysis to the noncritical profile because the primary objective of this paper is to study the critical profile. Therefore we proceed by using Eqs. (B1) and (B2) to obtain the result

$$\bar{\rho}_{\text{NC}}=\left[\frac{\varepsilon(+\infty,t)+1}{\varepsilon_i+1}\right]^{1/2}\frac{\varepsilon_i-1}{\varepsilon(+\infty,t)-1}\bar{\rho}_{\text{pure}}+\frac{\pi}{\lambda}\frac{\sqrt{\varepsilon(+\infty,t)+1}[\varepsilon(+\infty,t)-\varepsilon_i]}{\varepsilon(+\infty,t)-1}\times\int_{-\infty}^{0}[1-1/\varepsilon(z)]dz\ . \tag{B4}$$

We define the quantity

$$R_V(t)=-\frac{[\varepsilon(+\infty,t)-\varepsilon_i]\int_{-\infty}^{0}[1-1/\varepsilon(z)]dz}{\int_{-\infty}^{0}[\varepsilon(z)-\varepsilon_i][1-1/\varepsilon(z)]dz}\ . \tag{B5}$$

Use of Eq. (B2) shows that $R_V(t)$ is the ratio of the second term to the first in Eq. (B4). This provides the result

TABLE VII. Reduced temperature versus $\bar{\rho}$ data for the critical mixture NH (nitrobenzene–*n*-hexane).

t	$\bar{\rho}$ (10^{-3})	t	$\bar{\rho}$ (10^{-3})	t	$\bar{\rho}$ (10^{-3})
		NH one-phase region			
8.480×10^{-2}	2.519	7.881×10^{-3}	4.529	1.757×10^{-3}	6.368
6.775×10^{-2}	2.686	7.536×10^{-3}	4.598	1.423×10^{-3}	6.463
5.082×10^{-2}	2.864	7.199×10^{-3}	4.657	1.075×10^{-3}	6.702
3.410×10^{-2}	2.957	6.854×10^{-3}	4.737	9.177×10^{-4}	7.009
3.388×10^{-2}	3.147	6.786×10^{-3}	4.684	8.563×10^{-4}	7.021
3.068×10^{-2}	3.153	6.513×10^{-3}	4.850	7.949×10^{-4}	7.095
2.723×10^{-2}	3.242	6.168×10^{-3}	4.734	7.301×10^{-4}	6.981
2.380×10^{-2}	3.365	5.817×10^{-3}	4.764	7.301×10^{-4}	7.123
2.044×10^{-2}	3.501	5.466×10^{-3}	4.888	6.721×10^{-4}	7.148
1.702×10^{-2}	3.666	5.128×10^{-3}	5.141	6.243×10^{-4}	7.063
1.691×10^{-2}	3.739	4.797×10^{-3}	5.223	5.629×10^{-4}	7.080
1.364×10^{-2}	3.751	4.459×10^{-3}	5.307	5.015×10^{-4}	7.136
1.026×10^{-2}	4.251	4.125×10^{-3}	5.425	4.367×10^{-4}	7.188
1.023×10^{-2}	4.067	3.784×10^{-3}	5.312	3.923×10^{-4}	7.478
9.918×10^{-3}	4.280	3.456×10^{-3}	5.382	3.719×10^{-4}	7.126
9.580×10^{-3}	4.328	3.111×10^{-3}	5.522	3.139×10^{-4}	7.030
9.239×10^{-3}	4.379	2.777×10^{-3}	5.797	2.559×10^{-4}	6.878
8.901×10^{-3}	4.406	2.439×10^{-3}	5.974	1.945×10^{-4}	6.613
8.557×10^{-3}	4.325	2.098×10^{-3}	6.150	1.501×10^{-4}	6.249
8.219×10^{-3}	4.373				
		NH two-phase region			
2.207×10^{-2}	1.565	5.131×10^{-3}	2.295	6.482×10^{-4}	3.836
2.038×10^{-2}	1.583	3.439×10^{-3}	2.570	6.209×10^{-4}	4.039
1.869×10^{-2}	1.637	3.231×10^{-3}	2.571	5.902×10^{-4}	3.922
1.700×10^{-2}	1.685	3.013×10^{-3}	2.760	5.288×10^{-4}	4.001
1.530×10^{-2}	1.725	2.675×10^{-3}	2.904	4.708×10^{-4}	4.118
1.386×10^{-2}	1.787	2.334×10^{-3}	3.044	4.060×10^{-4}	4.230
1.361×10^{-2}	1.774	2.003×10^{-3}	3.016	3.480×10^{-4}	4.362
1.192×10^{-2}	1.846	1.658×10^{-3}	3.144	2.832×10^{-4}	4.732
1.120×10^{-2}	1.913	1.307×10^{-3}	3.477	2.798×10^{-4}	4.495
1.022×10^{-2}	1.924	9.621×10^{-4}	3.721	2.286×10^{-4}	4.676
8.522×10^{-3}	2.024	8.870×10^{-4}	3.572	1.706×10^{-4}	4.880
7.564×10^{-3}	2.125	8.265×10^{-4}	3.626	1.058×10^{-4}	5.124
6.830×10^{-3}	2.099	7.676×10^{-4}	3.701	4.435×10^{-5}	5.365
5.790×10^{-3}	2.569	7.096×10^{-4}	3.774	1.365×10^{-5}	5.606
5.141×10^{-3}	2.452				

TABLE VIII. Reduced temperature versus $\bar{\rho}$ data for the critical mixture PD (3-methylpyridine–D_2O).

t	$\bar{\rho}$ (10^{-3})	t	$\bar{\rho}$ (10^{-3})	t	$\bar{\rho}$ (10^{-3})
		PD one-phase region			
4.504×10^{-2}	−1.280	9.461×10^{-3}	−3.103	3.415×10^{-3}	−4.823
4.180×10^{-2}	−1.335	8.903×10^{-3}	−3.459	3.096×10^{-3}	−4.843
3.858×10^{-2}	−1.458	8.258×10^{-3}	−3.480	3.009×10^{-3}	−4.638
3.533×10^{-2}	−1.648	7.616×10^{-3}	−3.605	2.773×10^{-3}	−4.996
3.210×10^{-2}	−1.575	6.968×10^{-3}	−3.583	2.444×10^{-3}	−5.005
2.887×10^{-2}	−1.699	6.320×10^{-3}	−3.808	2.125×10^{-3}	−5.277
2.564×10^{-2}	−1.842	6.230×10^{-3}	−3.599	1.799×10^{-3}	−5.483
2.239×10^{-2}	−1.988	5.675×10^{-3}	−4.065	1.480×10^{-3}	−5.591
1.917×10^{-2}	−2.190	4.975×10^{-3}	−4.170	1.154×10^{-3}	−5.732
1.592×10^{-2}	−2.445	4.382×10^{-3}	−4.461	8.384×10^{-4}	−5.693
1.270×10^{-2}	−2.696	4.053×10^{-3}	−4.498	5.159×10^{-4}	−5.706
9.541×10^{-3}	−3.379	3.740×10^{-3}	−4.625	1.870×10^{-4}	−5.211
		PD two-phase region			
5.171×10^{-2}	0.068	1.948×10^{-2}	−0.196	3.360×10^{-3}	−1.157
4.849×10^{-2}	0.113	1.625×10^{-2}	−0.274	3.357×10^{-3}	−1.399
4.527×10^{-2}	0.137	1.303×10^{-2}	−0.460	2.705×10^{-3}	−1.658
4.205×10^{-2}	0.063	9.806×10^{-3}	−0.650	2.064×10^{-3}	−1.978
3.882×10^{-2}	0.178	6.581×10^{-3}	−0.992	1.093×10^{-3}	−2.591
3.560×10^{-2}	−0.017	5.940×10^{-3}	−0.970	7.739×10^{-4}	−3.113
3.237×10^{-2}	−0.071	5.295×10^{-3}	−1.070	4.514×10^{-4}	−3.866
2.914×10^{-2}	0.002	4.650×10^{-3}	−1.184	1.354×10^{-4}	−4.864
2.593×10^{-2}	−0.072	4.005×10^{-3}	−1.288	1.354×10^{-4}	−4.276
2.270×10^{-2}	−0.089				

$$\bar{\rho}_{\rm NC}\cong\left[\frac{\varepsilon(+\infty,t)+1}{\varepsilon_i+1}\right]^{1/2}\frac{\varepsilon_i-1}{\varepsilon(+\infty,t)-1}[1+R_V(t)]\bar{\rho}_{\rm pure}\ . \tag{B6}$$

Using Eq. (34) in Eq. (B5) gives

$$R_V(t)=\frac{[\varepsilon_i-\varepsilon(+\infty,t)]\ln\{\varepsilon_i[1+\exp(z_e/\xi_V)]\}}{(\varepsilon_i-1)\exp(-z_e/\xi_V)\ln[1+\exp(z_e/\xi_V)]-\varepsilon_i\ln(\varepsilon_i)}\ . \tag{B7}$$

As determined by Eq. (B7), $R_V(t)$ at $t=0$ is provided for each mixture in Table I. Though $R_V(t)$ is much too large to be neglected, the dependence of $\bar{\rho}_{\rm NC}$ in Eq. (B6) on the specific model noncritical profile has been reduced. In applying Eq. (B6) to the experimental data, $\bar{\rho}_{\rm pure}$ will be fitted as an adjustable parameter. $R_V(t)$ is only weakly dependent on t, therefore an inaccurate model noncritical profile should merely shift the fitted $\bar{\rho}_{\rm pure}$ value away from the measured value while introducing negligible error to the important fitted critical parameters $\int P_{\pm}$.

APPENDIX C: $(\bar{\rho},t)$ DATA

In Tables VI, VII, and VIII we provide the ellipsometric data for the mixtures LW, NH, and PD. These are our most reliable data sets in that criticality was verified for these three mixtures (see Sec. V). Sample preparation, ellipsometric measurement procedures, and the measured T_c values for these three samples are given in Ref. [17]. The temperature control had 0.5 mK stability for each data point, while the $\bar{\rho}$ measurements were reproducible to within an error of $\pm5\times10^{-5}$.

[1] E. Brezin, J. C. Le Guillou, and J. Zinn-Justin, Phys. Lett. **47A**, 285 (1974); H. B. Tarko and M. E. Fisher, Phys. Rev. Lett. **31**, 926 (1973); A. J. Liu and M. E. Fisher, Physica (Amsterdam) A **156**, 35 (1989).

[2] In the two-phase region careful theoretical consideration has only been given to the case of adsorption of the lighter component L at the liquid-vapor surface. To attempt to describe the adsorption profile for the case in which the heavier component H is preferentially adsorbed, one can construct the scaling equation

$$m_{\pm}(z,t)=M_{-}t^{\beta}\left[2P_{\pm}(\infty)-P_{\pm}\left[\frac{z+z_e}{\xi_{\pm}}\right]\right],$$

which reduces to Eq. (4) in the one-phase region and gives the correct exponential decay for $z \gg \xi_{\pm}$ in both the one- and the two-phase regions. This scaling form, however, experiences problems in the two-phase region for $z \ll \xi_{-}$ when, because $P_{-}(\infty)=1$ and using Eq. (8), the most singular critical term of $m_{-}(0,t)$ is t^{β} rather than $t^{2-\alpha}$ [10]. It thus seems that the case of desorption of component L at the liquid-vapor surface in the two-phase region cannot be correctly described by the scaling function $P_{-}(x)$ appearing in Eq. (2). The case of desorption seems to require the scaling equation

$$m_{\pm}(z,t)=-M_{-}t^{\beta}P_{\pm}\left[\frac{z+z_e}{\xi_{\pm}}\right],$$

with Eqs. (7) and (8) still holding, but with $P_{+}(\infty)=0$ and $P_{-}(\infty)=-1$.

[3] P. Kumar, Phys. Rev. B **10**, 2928 (1974); T. C. Lubensky and M. H. Ruben, *ibid.* **12**, 3885 (1975); K. Binder, in *Phase Transitions and Critical Phenomena,* edited by C. Domb and J. L. Lebowitz (Academic, London, 1983), Vol. VIII, p. 1; H. W. Diehl, in *Phase Transitions and Critical Phenomena,* edited by C. Domb and J. L. Lebowitz (Academic, London, 1986), Vol. X, p. 75; K. Ohno and Y. Okabe, Phys. Rev. B **39**, 9764 (1989).

[4] M. E. Fisher and P.-G. de Gennes, C. R. Acad. Sci. Paris B **287**, 207 (1978).

[5] See S. Dietrich, in *Phase Transitions and Critical Phenomena,* edited by C. Domb and J. Lebowitz (Academic, London, 1987), Vol. 12, Sec. IX B.

[6] A. J. Liu and M. E. Fisher, Phys. Rev. A **40**, 7202 (1989).

[7] M. Schlossman, X.-L. Wu, and C. Franck, Phys. Rev. B **31**, 1478 (1985).

[8] J. W. Schmidt, Phys. Rev. A **41**, 885 (1990).

[9] R. Sussmann and G. H. Findenegg, Physica (Amsterdam) A **156**, 114 (1989).

[10] H. W. Diehl and M. Smock, Phys. Rev. B **47**, 5841 (1993); **48**, 6470(E) (1993).

[11] M. Smock, H. W. Diehl, and D. P. Landau, Ber. Bunsenges. Phys. Chem. **98**, 486 (1994).

[12] D. P. Landau and K. Binder, Phys. Rev. B **41**, 4786 (1990).

[13] G. Flöter and S. Dietrich, Z. Phys. B **97**, 213 (1995).

[14] B. M. Law, C. M. Sorensen, F. Zhou, and J. V. Sengers, Fluid Phase Equil. **75**, 225 (1992).

[15] B. M. Law, Phys. Rev. Lett. **67**, 1555 (1991).

[16] B. M. Law, Phys. Rev. Lett. **69**, 1781 (1992).

[17] D. S. P. Smith and B. M. Law, J. Chem. Phys. **99**, 9836 (1993).

[18] T. W. Burkhardt and H. W. Diehl, Phys. Rev. B **50**, 3894 (1994).

[19] W. V. Andrew, T. B. K. Khoo, and D. T. Jacobs, J. Chem. Phys. **85**, 3985 (1986).

[20] D. Beaglehole, in *Fluid Interfacial Phenomena,* edited by C. A. Croxton (Wiley, New York, 1986).

[21] D. Beaglehole, Physica (Amsterdam) B **100**, 163 (1980).

[22] P. K. L. Drude, *The Theory of Optics* (Dover, New York, 1959), p. 292.

[23] M. Born and E. Wolf, *Principles of Optics* (Pergamon, Oxford, 1980), Sec. 1.6; B. M. Law and D. Beaglehole, J. Phys. D **14**, 115 (1981); B. M. Law, Ph.D. thesis, Victoria University of Wellington, New Zealand, 1985 (unpublished).

[24] D. S. P. Smith, B. M. Law, M. Smock, H. W. Diehl, and D. P. Landau (unpublished).

[25] P. R. Bevington, *Data Reduction and Error Analysis for the Physical Sciences* (McGraw-Hill, New York, 1969). Subroutine CURFIT of Chap. 11 is used for the nonlinear least-squares fit. The procedure used to calculate the error-weighted mean and standard deviation is from the bottom of p. 73. The formula for the error weighted mean given in Eq. (11) of Ref. [16] contains an extraneous factor of $1/N$.

[26] C. Caylor, D. S. P. Smith, and B. M. Law (unpublished).

[27] See, for example, J. W. Schmidt and M. R. Moldover, J. Chem. Phys. **99**, 582 (1993), V. L. Kuzmin and V. P. Romanov, Phys. Rev. E **49**, 2949 (1994), and references therein.

[28] *CRC Handbook of Chemistry and Physics,* 63rd ed., edited by Robert C. Weast (Chemical Rubber Company, Boca Raton, FL, 1982).

[29] D. Beysens, A. Bourgou, and P. Calmettes, Phys. Rev. A **26**, 3589 (1982).

[30] D. Atack and O. K. Rice, Discuss. Faraday Soc. **15**, 210 (1953).

[31] P. Calmettes, I. Lagues, and C. Laj, Phys. Rev. Lett. **28**, 478 (1972).

[32] G. Morrison and C. M. Knobler, J. Chem. Phys. **65**, 5507 (1977).

[33] D. Beysens and D. Esteve, Phys. Rev. Lett. **54**, 2124 (1985).

[34] M. A. Handschy, R. C. Mockler, and W. J. O'Sullivan, Chem. Phys. Lett. **76**, 172 (1980). The first 15 data points were refitted with $\beta=0.325$ to give $\Delta n=0.288t^{\beta}$.

[35] E. Gulari, A. F. Collings, R. L. Schmidt, and C. J. Pings, J. Chem. Phys. **56**, 6169 (1972). Gulari *et al.* measured 2.0 ± 0.2 and 2.92 ± 0.19 Å for the correlation length. In Ref. [23] we find that 2.5 Å works well.

[36] G. Zalcer, A. Bourgou, and D. Beysens, Phys. Rev. A **28**, 440 (1983).

[37] J. Rouch, P. Tartaglia, and S. H. Chen, Phys. Rev. A **37**, 3046 (1988).

[38] The volume coexistence curve was estimated from the graph in J. D. Cox, J. Chem. Soc. (London) **1952**, 4606 (1952).

[39] C. Houessou, P. Guenoun, R. Gastaud, F. Perrot, and D. Beysens, Phys. Rev. A **32**, 1818 (1985).

[40] I. L. Pegg, Ph.D. thesis, University of Sheffield, 1982 (unpublished).

[41] Obtained by fitting the data provided in Ref. 8.

[42] Y. Jayalakshmi, J. S. Van Duijneveldt, and D. Beysens, J. Chem. Phys. **100**, 604 (1994).

[43] The Clausius-Mossotti equation (24) has been used to convert the coexistence curve to refractive index.